

Unified Primitive Proxies for Structured Shape Completion

Zhaiyu Chen^{1,2}

Yuqing Wang¹

Xiao Xiang Zhu^{1,2}

¹Technical University of Munich

²Munich Center for Machine Learning

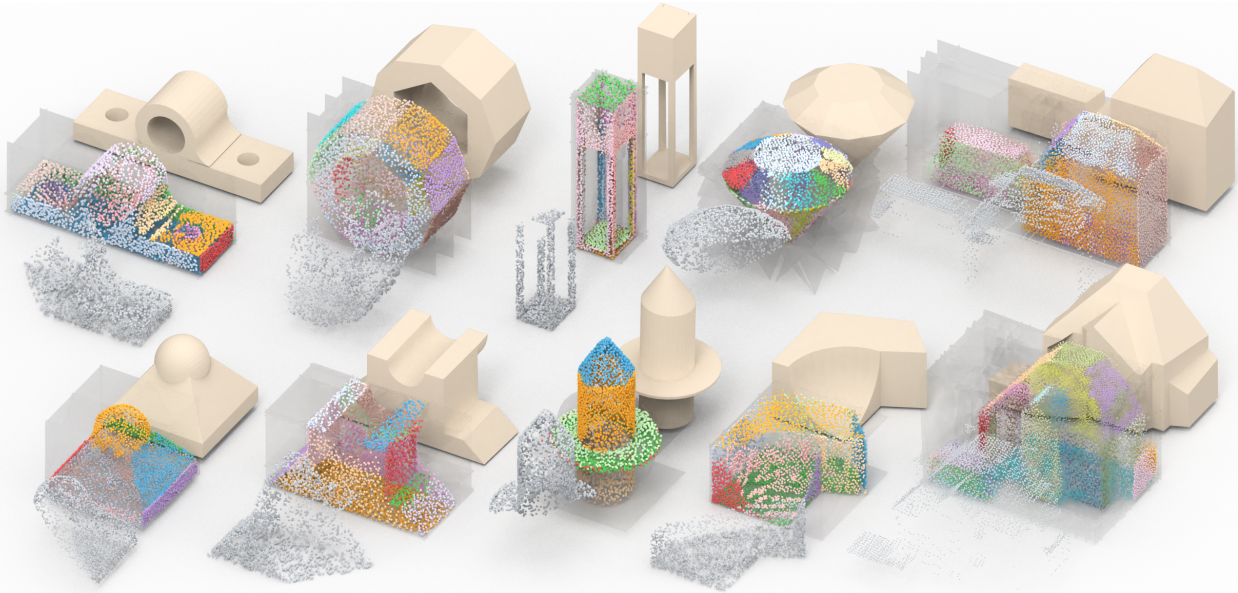


Figure 1. We present *UniCo*, a structured shape completion model that, given a partial scan, jointly predicts a complete set of quadratic primitives with geometry, semantics, and inlier membership. The predicted primitives are assembly-ready for surface reconstruction.

Abstract

Structured shape completion recovers missing geometry as primitives rather than as unstructured points, which enables primitive-based surface reconstruction. Instead of following the prevailing cascade, we rethink how primitives and points should interact, and find it more effective to decode primitives in a dedicated pathway that attends to shared shape features. Following this principle, we present UniCo, which in a single feed-forward pass predicts a set of primitives with complete geometry, semantics, and inlier membership. To drive this unified representation, we introduce primitive proxies, learnable queries that are contextualized to produce assembly-ready outputs. To ensure consistent optimization, our training strategy couples primitives and points with online target updates. Across synthetic and real-world benchmarks with four independent assembly solvers, UniCo consistently outperforms recent baselines, lowering Chamfer distance by up to 50% and improving normal consistency by up to 7%. These results establish an attractive recipe for structured 3D understanding from incomplete data. Project page: <https://unico-completion.github.io>.

1. Introduction

Occlusions and limited sensor coverage often leave 3D scans incomplete. Completing the missing geometry allows robots to plan stable grasps, enables autonomous vehicles to perceive hidden traffic, and supports digitizing heritage artifacts without repeated acquisitions [47, 51, 53, 73].

Despite advances, most shape completion methods still optimize pointwise discrepancies [69–71] or their variants [34, 35, 57]. These objectives capture local geometry but convey little about the structural regularities required by many downstream tasks [2, 24]. In contrast, primitive assembly models the surface as a compact, topologically consistent collection of parametric primitives for structured, interpretable geometry [1, 20, 38, 45]. However, the common recipe of completing first and assembling later is underconstrained, because assembly solvers expect structured input that pointwise completion does not provide. It is therefore preferable to predict structure jointly with completion.

Toward structured shape completion that directly supports

primitive assembly, a straightforward approach is a two-stage cascade that first regresses primitive parameters and then enforces inlier points, typically limited to plane-only primitives [10]. In practice, this rigid formulation tends to overfit well-supported regions and degrade when evidence is sparse. It can also propagate early errors in primitive count or parameters into the association step, which weakens later supervision. These limitations motivate a formulation in which point completion and primitive inference are optimized in a more coordinated way.

How can primitives be optimized more effectively? We follow three design principles: ① *Coordinated pathways*. Point completion and primitive inference are driven by different supervision signals, since the former benefits from pointwise guidance whereas the latter relies on discrete and relational cues. We therefore let completion run in its own pathway and decode primitives in parallel from shared features. ② *Unified representation*. Structural information is dispersed across the shared features, which makes coordination nontrivial. We introduce primitive proxies that attend to these shared features and provide a unified representation that binds evidence to candidate primitives. ③ *Consistent optimization*. Early in training, the predicted point distribution is not accurate enough to support reliable primitive membership. We therefore update primitive targets online, while keeping the matching permutation-invariant, so that both pathways maintain stable training dynamics.

Following these principles, we present UniCo, a structured shape completion model that predicts assembly-ready quadratic primitives with complete geometry, semantics, and inlier membership in a single pass. UniCo is purpose-built to enable reliable primitive assembly from challenging incomplete data. To summarize, our contributions are:

- *Formulation*. We rethink how primitives and points should be coordinated and introduce UniCo, a structured shape completion model that jointly optimizes both, producing assembly-ready primitives in one pass.
- *Representation*. We present primitive proxies as learnable queries over shared features that produce a unified primitive representation and jointly drive geometry, semantics, and inlier membership predictions.
- *Optimization*. We develop a training strategy with online target updates for consistent support between primitives and points as predictions evolve.

These contributions realize our design principles in a single versatile solution. UniCo supports multiple primitive families and includes a planar variant for cases dominated by planar structures. On three benchmarks covering synthetic and real scans, and evaluated with four assembly solvers, UniCo consistently outperforms recent baselines, lowering Chamfer distance by up to 50% and improving normal consistency by up to 7%. We hope these findings stimulate further work on structured 3D understanding from incomplete data.

2. Related Work

3D shape completion. Early approaches to shape completion used volumetric CNNs, but voxel representations suffer from discretization artifacts and high memory costs at fine resolutions [12, 17, 60, 62]. The introduction of PointNet enabled direct processing of unordered point sets [39], which led to a broad family of point-based completion networks [40, 50, 55]. Most recent methods, including PoinTr [69], AdaPoinTr [70], ODGNet [3], SymmComplete [63], and others [8, 29, 48, 49, 61, 65, 66, 71, 72, 74], still minimize pointwise discrepancies or their variants [34, 35, 57], so they recover local geometry but leave higher-level structure underconstrained. PaCo moves toward structured shape completion by first predicting plane parameters and then enforcing inlier membership in a cascade, yet this design remains sensitive to sparse evidence and early errors, and is restricted to plane-only primitives [10]. In contrast, our approach unifies shape completion and structural reasoning in a single network with coordinated pathways, enabling consistent optimization across multiple primitive families.

Primitive assembly. Unlike generic surface reconstruction that targets dense meshes [14, 18, 19, 23], primitive assembly reconstructs surfaces by arranging primitives under geometric and topological constraints. Although recent neural approaches explore learned decompositions and constructive modeling [6, 31, 36, 41, 52, 67], primitive assembly remains the practical standard when topology control, editability, and compatibility are required [2, 5, 7, 9, 22]. Representative solvers include PolyFit [38], KSR [1], and COMPOD [45] for polygonal surfaces, and PrimFit [20] for more general primitive families. However, their performance degrades under partial observations because assembly depends on reliable, complete primitives, which motivates learning structured representations from partial scans that supply assembly-ready primitives.

Primitive extraction. Primitive extraction is often cast as instance segmentation. Traditional pipelines rely on geometric model fitting and constraints, but lack learned inductive biases [32, 42, 68]. Learning-based methods later adopted a clustering paradigm, where a shared backbone first produces pointwise features and a subsequent stage groups points into primitive instances [28, 30, 44, 64]. This paradigm led benchmarks for several years [4, 21, 26, 33, 54]. More recent Transformer-based models predict masks directly with instance queries and avoid hand-crafted grouping [27, 37, 43, 46]. However, they rarely encode primitive-specific priors and typically assume complete, fixed point sets, which hinders transfer to completion settings with inconsistent targets. In contrast, we infer primitives in tandem with completion, jointly predicting memberships from incomplete scans while reasoning about missing geometry.

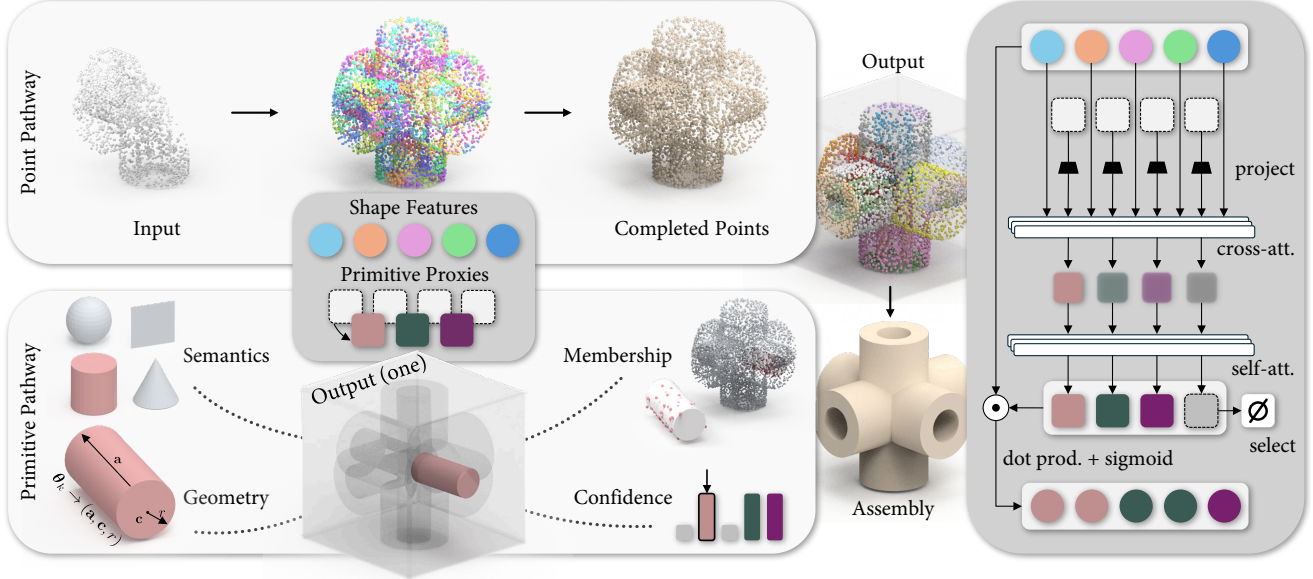


Figure 2. **Architecture of UniCo.** Shape features from a partial point cloud feed two coordinated pathways. The *point pathway* decodes dense completed points. The *primitive pathway* uses primitive proxies that attend to the shared features and predict primitive semantics, geometry, inlier membership, and a confidence score used at inference to select valid primitives. The selected primitives are assembly-ready.

3. Method

Given a partial point cloud, we complete the shape by jointly predicting a point set and a primitive set with geometry, semantics, and inlier membership, yielding an assembly-ready representation of the complete object. Fig. 2 illustrates the architecture. We extract shape features from the input points. The point pathway decodes dense points, while the primitive pathway contextualizes a fixed set of primitive proxies from the shared features to predict candidate primitives. During training, we update primitive targets online and use permutation-invariant matching to keep supervision aligned with evolving predictions. At inference, confidence scores select the valid subset of primitives.

3.1. Coordinated Pathways

The point pathway reconstructs dense geometry, while the primitive pathway infers structural elements that abstract the object into parametric primitives. Both pathways share the same latent features $\mathcal{T} = \{\mathbf{t}^u\}_{u=1}^U$, which promotes consistency between fine-grained point completion and higher-level primitive prediction.

Point pathway. We instantiate the point pathway f_{point} with AdaPoinTr [70], though in principle any pointwise shape completion network could be used. This pathway recovers a local point patch from each feature \mathbf{t}^u and aggregates them into the completed points $\hat{\mathcal{Y}} \subset \mathbb{R}^3$:

$$\hat{\mathcal{Y}} = f_{\text{point}}(\mathcal{T}) = \bigcup_{u=1}^U \hat{\mathcal{Y}}^u, \quad \hat{\mathcal{Y}}^u = \{\hat{\mathbf{y}}_j^u\}_{j=1}^J, \quad (1)$$

where $\hat{\mathbf{y}}_j^u$ denotes a point in the patch decoded from \mathbf{t}^u .

Primitive pathway. In parallel, the primitive pathway $f_{\text{primitive}}$ employs a set of primitive proxies $\mathcal{R} \subset \mathbb{R}^d$, which are contextualized against the same features:

$$\mathcal{R} = f_{\text{primitive}}(\mathcal{T}, \mathcal{R}^{(0)}) = \{\mathbf{r}_k\}_{k=1}^K, \quad (2)$$

where $\mathcal{R}^{(0)}$ denotes the initialized proxies and \mathcal{R} the contextualized ones. The embeddings are subsequently processed by dedicated prediction heads.

3.2. Primitive Proxies

We introduce primitive proxies, learnable queries that aggregate dispersed structural cues from the shape features into unified primitive-level representations. A fixed set of proxies is contextualized with the shared shape features and then decoded by the geometry, semantics, and membership heads.

Contextualization. The primitive proxies are initialized as queries $\mathcal{R}^{(0)}$. At layer l , they attend to the shared shape features \mathcal{T} and then interact among themselves:

$$\mathcal{R}^{(l)} = \text{self-att}(\text{cross-att}(\mathcal{R}^{(l-1)}, \text{MLP}(\mathcal{T}))). \quad (3)$$

The final contextualized proxies $\mathcal{R} = \{\mathbf{r}_k\}_{k=1}^K$ are shared across the prediction heads. Fig. 2 illustrates this process.

Semantics. For mixed-type settings, an MLP classification head predicts the type of each primitive candidate:

$$\boldsymbol{\pi}_k = \text{softmax}(\text{MLP}(\mathbf{r}_k)), \quad (4)$$

where $\boldsymbol{\pi}_k$ is a categorical distribution over five classes (plane, cylinder, sphere, cone, \emptyset), with \emptyset denoting noncontributing

candidates. The formulation can extend to additional primitive families, provided the downstream solver supports them. In plane-only settings, Eq. (4) reduces to a binary classifier.

Membership. Each primitive candidate predicts its inlier subset among the completed points. Given a primitive proxy \mathbf{r}_k and a shape feature \mathbf{t}^u , we compute their pairwise similarity in a shared latent space:

$$m_k^u = \text{sigmoid}(\langle \text{MLP}(\mathbf{r}_k), \text{MLP}(\mathbf{t}^u) \rangle), \quad (5)$$

where both $\text{MLP}(\cdot)$ project into the same latent space, and $\langle \cdot, \cdot \rangle$ denotes the dot product. Inlier points for primitive k are then obtained by thresholding:

$$\hat{\mathcal{I}}_k = \{u \mid m_k^u > 0.5\}. \quad (6)$$

All similarity scores are stacked into a membership matrix $\mathbf{M} \in [0, 1]^{K \times U}$ for optimization.

Geometry. The geometry head maps each contextualized proxy \mathbf{r}_k to quadric parameters, providing a unified homogeneous parametrization for common primitives: $\boldsymbol{\theta}_k := \mathbf{A}_k = \text{MLP}(\mathbf{r}_k)$. The corresponding surface is defined as:

$$\mathbf{x}^\top \mathbf{A}_k \mathbf{x} = 0, \quad \mathbf{A}_k = \mathbf{A}_k^\top \in \mathbb{R}^{4 \times 4}, \quad (7)$$

where \mathbf{x} denotes the homogeneous coordinates of a point on the surface. For plane-only settings, we set $[\mathbf{A}_k]_{1:3, 1:3} = \mathbf{0}$ to avoid ambiguity. We also derive the dense point geometry for each primitive using its predicted membership:

$$\hat{\mathcal{Y}}_k = \bigcup_{u \in \hat{\mathcal{I}}_k} \hat{\mathcal{Y}}^u. \quad (8)$$

3.3. Optimization

Unlike standard primitive learning on fixed point sets with direct membership supervision, our predicted points evolve during training, so a fixed point-to-membership correspondence would be ill-defined. We therefore induce membership supervision online: at each iteration we assign ground truth primitive labels to the current predictions and train on these induced labels. To align the unordered set of predicted primitives with targets, we compute the loss after permutation-invariant matching. As training progresses, both the induced memberships and the matching are updated, resulting in a self-consistent optimization loop.

Online targets. We first assign labels to the predicted points. Given the ground-truth point set $\mathcal{Y} = \{\mathbf{y}_i\}_{i=1}^N$ with primitive labels $\mathcal{P} = \{p_i\}_{i=1}^N$, where $p_i \in \{1, \dots, G\}$ denotes the primitive index of point i . Each predicted point $\hat{\mathbf{y}}_j^u$ takes the label of its nearest ground-truth neighbor:

$$\hat{p}_j^u = p_{i^*}, \quad i^* = \arg \min_i \|\hat{\mathbf{y}}_j^u - \mathbf{y}_i\|_2. \quad (9)$$

The patch-level primitive label is then obtained by a majority vote of these assigned point labels:

$$\hat{\mathcal{P}}^u = \arg \max_g \sum_{j=1}^J \mathbb{1}\{\hat{p}_j^u = g\}, \quad (10)$$

where $\mathbb{1}\{\cdot\}$ is the indicator function and g indexes a primitive. For each primitive, we collect the patches assigned to it:

$$\mathcal{I}_g = \{u \mid \hat{\mathcal{P}}^u = g\}, \quad (11)$$

and use these sets as online targets to supervise the primitive-specific predictions. The targets are recomputed at every iteration, allowing assignments and network parameters to be optimized jointly during training.

Matching and losses. To align the unordered predicted primitives with ground-truth primitives, we establish a pairwise cost and solve a bipartite assignment:

$$\begin{aligned} \text{cost}(k, g) = & -\alpha_1 \underbrace{\log \pi_k[c_g]}_{\text{semantics}} + \alpha_2 \underbrace{(\text{CE} + \text{Dice})(\mathbf{M}_k, \mathcal{I}_g)}_{\text{membership}} \\ & + \alpha_3 \underbrace{[\text{CD}(\hat{\mathcal{Y}}_k, \mathcal{Y}_g) + \lambda \|\boldsymbol{\theta}_k - \boldsymbol{\theta}_g\|_1]}_{\text{geometry}}. \end{aligned} \quad (12)$$

Here, $\alpha_1, \alpha_2, \alpha_3$ and λ are balancing weights. The semantic term encourages correct primitive type prediction. The membership term enforces point-primitive membership consistency using cross-entropy and Dice losses [13]. The geometry term aligns predicted inliers with the ground truth in both Chamfer distance and parameters. The optimal bipartite matching \mathcal{M} is obtained with the Hungarian algorithm [25]. The overall loss combines the matched primitive costs with an object-level distance from the point pathway:

$$\mathcal{L}_{\text{total}} = \sum_{(k^*, g^*) \in \mathcal{M}} \text{cost}(k^*, g^*) + \text{CD}(\hat{\mathcal{Y}}, \mathcal{Y}). \quad (13)$$

Unmatched predictions are downweighted via the semantic term to mitigate class imbalance.

Inference. At inference time, inspired by practices in instance segmentation [11, 43], we score each predicted primitive by combining its semantic confidence with the reliability of its inliers:

$$s_k = \pi_k[\hat{c}_k] \cdot \frac{1}{|\hat{\mathcal{I}}_k|} \sum_{u \in \hat{\mathcal{I}}_k} m_k^u, \quad (14)$$

where $\hat{c}_k = \arg \max_{c \neq \emptyset} \pi_k[c]$.

Primitives with $s_k > 0.5$ are retained and passed to the downstream assembly solver. Architectural and implementation details are provided in the [Appendix](#).

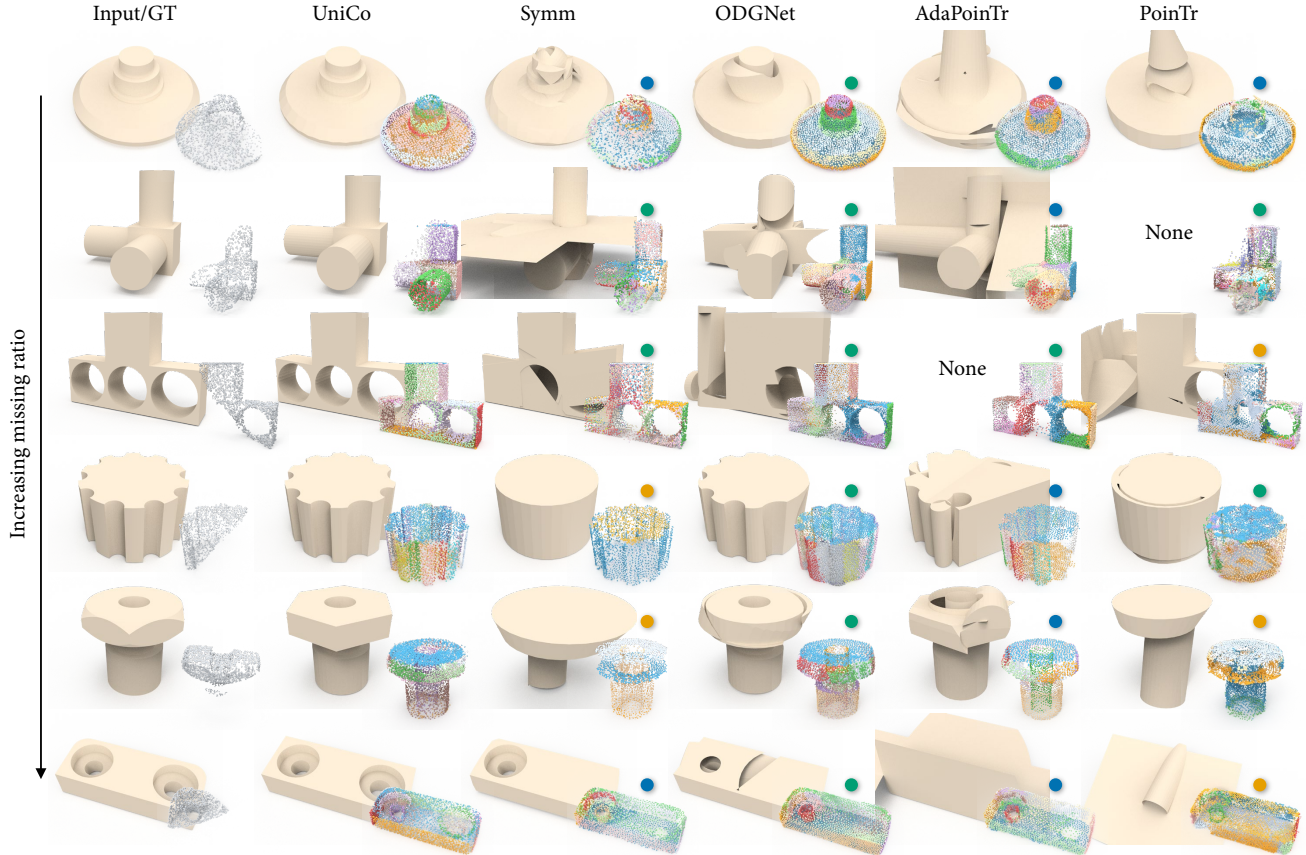


Figure 3. **Comparison to completion baselines on ABC-multi.** For each baseline, completed points are paired with its best-performing primitive extractor (● RANSAC [42], ● HPNet [64], ● PTv3 [59]). UniCo recovers extractor-free, assembly-ready primitive structures.

4. Experiments

4.1. Setup and Protocol

Datasets. We evaluate on three datasets for a comprehensive assessment. *ABC-multi* is a curated subset of 30,000 watertight CAD models from the ABC dataset [24], with 5,000 reserved for evaluation. It spans planes, cylinders, spheres, and cones, stressing completion with mixed primitive types. *ABC-plane* [10] is an existing plane-only dataset with over 15,000 CAD models. We use it to assess behavior in plane-dominant settings and to compare with polygonal pipelines. For real-world evaluation, we use *Building-PCC* [15], an airborne LiDAR dataset of about 50,000 urban buildings with realistic noise and occlusions. Following prior works [10, 70], *ABC-multi* and *ABC-plane* use 2,048 input points down-sampled from partial points at 25%, 50%, and 75% incompleteness, and 8,192 target points per shape, while *Building-PCC* uses native point counts.

Baselines and solvers. We compare three groups of baselines. For *completion*, we evaluate GRNet [62], PoinTr [69], AdaPoinTr [70], ODGNet [3], SymmComplete [63], and PaCo [10]. Unless stated otherwise, all methods are trained

to convergence. For *primitive extraction*, on *ABC-multi* we fit primitives to completed points using RANSAC [42], HPNet [64], and PTv3 [59], followed by PrimFit [20] for assembly. On *ABC-plane* and *Building-PCC*, we use GoCoPP [68] to extract primitives and then apply PolyFit [38], KSR [1], and COMPOD [45] for assembly. For *reconstruction*, we include BSP-Net [6] and Point2CAD [36], evaluated on both raw and completed points. For multi-stage pipelines (e.g., completion followed by reconstruction), we compose best models at each stage to obtain competitive baselines.

Metrics. Unless stated otherwise, evaluations are conducted on reconstructed meshes using Chamfer distance (CD), Hausdorff distance (HD), and normal consistency (NC). We also report the solver failure rate (FR), defined as the fraction of samples for which reconstruction fails. Additional metrics and setup details are provided in the [Appendix](#).

4.2. Mixed-Type Primitive Results

Structured vs. pointwise. On *ABC-multi* with the PrimFit solver, UniCo predicts primitives directly and reaches CD 2.18, HD 7.53, and NC 0.935, as reported in Tab. 1. This corresponds to 40–50% lower reconstruction error than the

Table 1. **Comparison with completion baselines on *ABC-multi***. Best scores are **bold**, second best are underlined. Baseline methods require a separate primitive extractor, whereas UniCo produces structured completion directly. All results are reconstructed with the same PrimFit solver [20]. CD, HD, and FR values are scaled by 100.

Method	Pointwise		RANSAC [42]				HPNet [64]				PTv3 [59]			
	CD	F1	CD ↓	HD ↓	NC ↑	FR ↓	CD ↓	HD ↓	NC ↑	FR ↓	CD ↓	HD ↓	NC ↑	FR ↓
GRNet [62]	1.177	0.565	18.61	24.71	0.543	100.00	18.61	24.71	0.543	100.00	18.61	24.71	0.543	100.00
PoinTr [69]	0.719	0.764	6.58	22.62	0.814	17.07	7.56	21.38	0.779	26.70	6.58	19.41	0.791	11.27
AdaPoinTr [70]	<u>0.625</u>	0.824	6.81	<u>21.24</u>	0.815	19.77	4.41	<u>13.36</u>	0.872	8.97	5.58	16.80	0.821	9.83
ODGNet [3]	0.632	0.850	<u>4.80</u>	22.15	<u>0.868</u>	0.39	<u>4.33</u>	13.63	<u>0.873</u>	<u>7.41</u>	<u>5.48</u>	<u>16.79</u>	<u>0.823</u>	<u>9.18</u>
SymmComplete [63]	0.487	<u>0.825</u>	7.54	21.42	0.796	26.13	4.57	13.58	0.865	9.84	5.93	17.58	0.812	11.50
UniCo (ours)	0.686	0.799	2.18	7.53	0.935	<u>1.49</u>	2.18	7.53	0.935	1.49	2.18	7.53	0.935	1.49

strongest competing method, ODGNet with HPNet, while also improving normal consistency. We repeat UniCo’s row across primitive extractor columns to show the gain is consistent. Notably, higher pointwise scores do not guarantee better reconstruction. SymmComplete attains the best pointwise CD and ODGNet the best pointwise F1, yet both still yield lower-quality meshes. As visualized in Fig. 3, UniCo produces cleaner, solver-aligned primitive layouts.

Assembly vs. reconstruction. As shown in Tab. 2, directly reconstructing meshes from partial inputs leads to high geometric errors. Supplying the best pointwise completion (ODGNet) as input to Point2CAD reduces these errors, yet UniCo still achieves substantially better reconstruction, lowering CD by about 36% and HD by 37%, while also improving NC. Fig. 4 visualizes the gap: BSP-Net collapses to coarse convex structures, Point2CAD introduces topological breaks, while UniCo’s assembly results preserve detail and maintain topological consistency.

Table 2. **Comparison with reconstruction methods**. Proc.: R = direct reconstruction; C→R = completion then reconstruction.

Method	Proc.	CD ↓	HD ↓	NC ↑	FR ↓
PrimFit [20]	R	7.80	25.17	0.788	15.96
Point2CAD [36]	R	8.69	30.66	0.779	15.91
BSP-Net [6]	R	8.35	16.73	0.740	20.52
CARPRI-Net [67]	R	7.59	15.18	0.770	19.27
Point2CAD [36]	C→R	<u>3.39</u>	<u>11.96</u>	<u>0.833</u>	0.66
UniCo (ours)	C→R	2.18	7.53	0.935	<u>1.49</u>



Figure 4. **Comparison with reconstruction methods**. Even with completed points with better pointwise metric, both competitors cannot produce detailed and robust reconstructions.

Robustness to missing, transforms, and noise. We stress-test UniCo under increasing incompleteness, a debiased normalization, and Gaussian jitter, as presented in Fig. 5. All networks are trained for 200 epochs. As incompleteness rises from 25% to 75%, UniCo’s CD increases only from 1.8 to 2.7, whereas strong pointwise baselines double their error to about 6.0. NC for UniCo drops from 0.95 to 0.91, whereas the baselines drop to 0.82. Under a debiased normalization that removes pose and scale canonicalization [56], UniCo degrades to CD 3.9 with NC 0.88, whereas the baselines deteriorate to CD above 14 with NC below 0.65, indicating that UniCo carries substantially less pose and scale bias. With Gaussian noise up to 3%, UniCo remains stable. At a heavy 5% noise level, CD and NC degrade to 3.2 and 0.88, respectively. Fig. 6 further shows view-to-view consistency, where different partial inputs yield a consistent primitive set that supports reliable assembly.

Primitive quality analysis. To better understand what drives the strong assembly performance, we further evaluate primitive quality following the established protocol [16, 30, 36]. For all competing methods, primitives are extracted with HPNet [64] for a feasible and fair comparison. Predicted primitives are then matched to ground truth via Hungarian matching. As shown in Tab. 3, we report F-Score@1% (F1), type accuracy (Type), axis difference (Axis), residual error (Res), and coverage (Cov). Axis measures the plane normal or the symmetry axis of cylinders and cones. Res evaluates the fit on 512 points sampled from the ground truth primitive. Cov is the fraction of these points that lie within a distance of 0.01 from the predicted primitive. UniCo attains the best scores on all primitive metrics, consistent with its stronger reconstruction performance.

Table 3. **Primitive quality**. Type, Res, and Cov are scaled by 100. Axis is in degrees. UniCo delivers higher-quality primitives.

Method	F1 ↑	Type ↑	Axis ↓	Res ↓	Cov ↑
GRNet [62]	0.215	29.65	25.97	7.12	24.41
PoinTr [69]	0.509	64.41	18.24	2.86	61.60
AdaPoinTr [70]	0.643	<u>79.79</u>	<u>11.34</u>	1.48	<u>78.99</u>
ODGNet [3]	<u>0.659</u>	75.52	12.24	1.78	75.85
SymmComplete [63]	0.629	78.48	12.72	1.54	77.60
UniCo (ours)	0.712	94.85	3.29	0.55	92.41

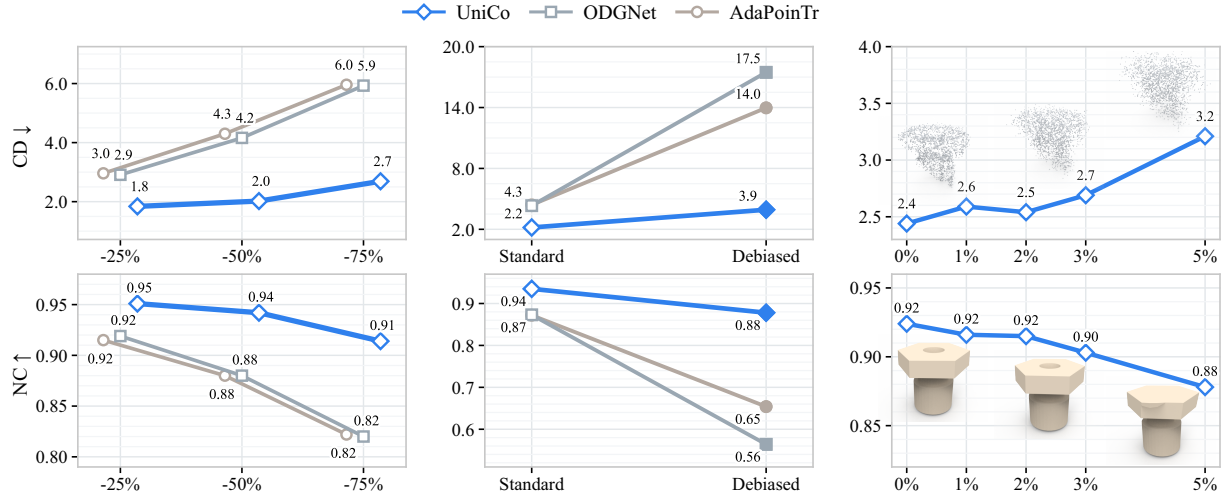


Figure 5. **Robustness to missing data, transforms, and noise.** Left: as incompleteness grows from 25% to 75%, UniCo maintains lower CD and higher NC than pointwise baselines. Middle: under the debaised normalization protocol [56], UniCo remains stable with low pose and scale bias compared to baselines. Right: under Gaussian jitter of 1–3%, performance degrades gracefully.

Table 4. **Comparison on ABC-plane.** UniCo achieves leading performance across three assembly solvers for polygonal surface reconstruction.

Method	Year	PolyFit [38]				KSR [1]				COMPOD [45]			
		CD ↓	HD ↓	NC ↑	FR ↓	CD ↓	HD ↓	NC ↑	FR ↓	CD ↓	HD ↓	NC ↑	FR ↓
GRNet [62]	2020	11.98	19.84	0.769	29.61	9.18	22.01	0.822	10.82	14.19	25.72	0.738	13.15
PoinTr [69]	2021	10.57	16.43	0.822	25.92	8.14	16.33	0.780	30.90	7.82	16.44	0.774	31.34
AdaPoinTr [70]	2023	3.16	7.36	0.920	5.89	3.24	8.86	0.927	0.27	3.25	8.84	0.921	1.32
ODGNet [3]	2024	2.73	6.41	0.933	4.28	2.90	8.56	0.934	0.36	3.22	8.01	0.927	1.05
SymmComplete [63]	2025	3.21	9.15	0.920	4.27	4.23	14.21	0.907	0.38	4.56	14.02	0.895	4.14
PaCo [10]	2025	<u>1.87</u>	4.09	<u>0.943</u>	0.48	<u>1.91</u>	4.14	<u>0.940</u>	<u>0.25</u>	<u>1.94</u>	<u>4.42</u>	<u>0.940</u>	<u>0.25</u>
UniCo (ours)	-	1.69	<u>4.28</u>	0.953	<u>0.69</u>	1.78	<u>4.59</u>	0.951	0.00	1.63	4.27	0.952	0.00

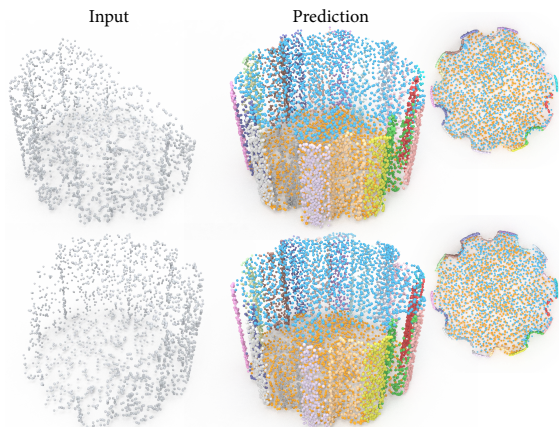


Figure 6. **Feature consistency.** From different partial views, UniCo predicts a consistent set of primitives representing the complete geometry. Matching colors denote identical primitive indices.

4.3. Planar Primitive Results

Specialization with minimal change. We reduce the semantic head in Eq. (4) to a binary classifier and replace the geometry head that predicts quadric coefficients with one that predicts plane parameters, leaving the rest of the architecture and training unchanged, which results in a strong model for plane-dominant scenarios. On *ABC-plane*, UniCo achieves

the lowest CD and highest NC across PolyFit, COMPOD, and KSR, as presented in Tab. 4. HD is best with COMPOD and second best with PolyFit and KSR, and the failure rate is even zero with both COMPOD and KSR. The planar primitives facilitate polygonal surface reconstruction more effectively than unstructured, pointwise completions, so the reconstructed surfaces are clean and well aligned.

Performance on real scans. On *Building-PCC*, UniCo delivers strong reconstruction results, as presented in Tab. 5. It achieves the best CD across all three solvers and the lowest failure rates. With PolyFit it also reaches the highest NC and a competitive HD, and with COMPOD it leads all three metrics. Fig. 7 presents qualitative results with PolyFit, showing roof superstructures with fewer distortions and preserving structural integrity across diverse architectural styles.

Joint vs. cascaded. Compared with the cascaded baseline PaCo, UniCo yields cleaner primitives with better support and hence more reliable reconstructions. On *ABC-plane*, it improves CD and NC across all three solvers, e.g. with COMPOD CD drops from 1.94 to 1.63 and FR from 0.25 to 0.00, as reported in Tab. 4. *Building-PCC* is more challenging, with many small and detailed structures, yet UniCo again excels across all metrics, e.g. with PolyFit the CD decreases

Table 5. **Comparison on Building-PCC.** On real LiDAR scans, UniCo produces the most reliable reconstructions across three solvers.

Method	PolyFit [38]				KSR [1]				COMPOD [45]			
	CD ↓	HD ↓	NC ↑	FR ↓	CD ↓	HD ↓	NC ↑	FR ↓	CD ↓	HD ↓	NC ↑	FR ↓
AdaPoinTr [70]	4.87	10.61	0.934	0.85	4.50	9.56	0.939	0.07	5.92	18.94	0.917	0.15
ODGNet [3]	3.97	9.09	<u>0.947</u>	0.87	4.41	<u>9.88</u>	0.947	0.61	<u>4.71</u>	13.81	<u>0.940</u>	1.77
SymmComplete [63]	7.55	14.74	0.893	24.98	13.09	24.45	0.803	38.94	9.73	22.54	0.878	20.48
PaCo [10]	4.89	10.74	0.932	<u>0.54</u>	4.47	10.20	0.934	0.17	<u>4.71</u>	<u>11.73</u>	0.932	0.00
UniCo (ours)	3.84	<u>9.18</u>	0.949	0.39	4.19	10.67	<u>0.944</u>	0.00	4.08	10.81	0.941	0.00

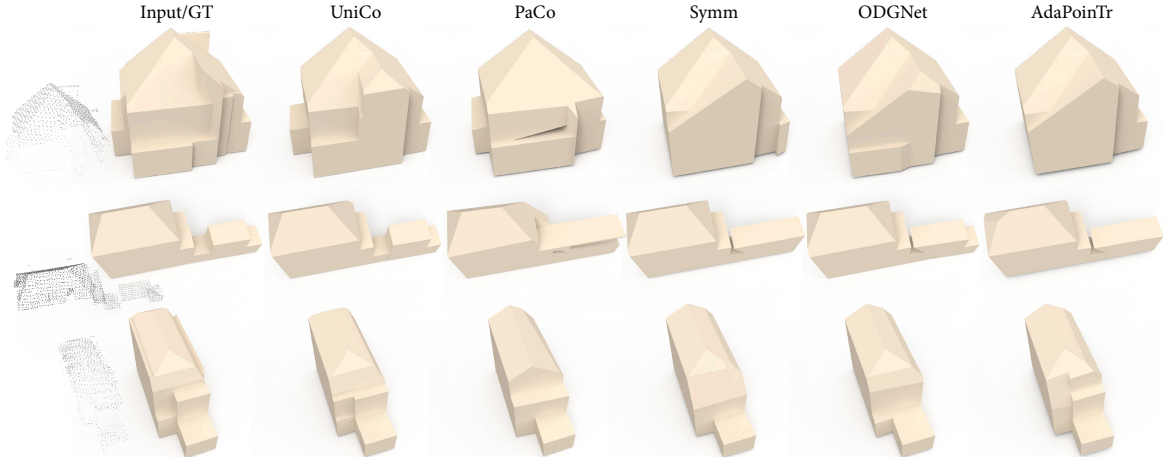


Figure 7. **Building reconstruction from real LiDAR scans.** UniCo recovers superstructures with higher fidelity.

from 4.89 to 3.84, as reported in Tab. 5. These results highlight that the coordinated pathways for learning primitives and points jointly are more effective than a cascaded design. Additional analysis is provided in the Appendix.

Table 6. **Ablation results.** “†” parameter head is required by solvers that depend on explicit parameters.

Variant	CD ↓	NC ↑
<i>Heads</i>		
no param. head†	2.52 (−0.08)	0.921 (−0.003)
no prim. chamfer	2.53 (−0.09)	0.920 (−0.004)
<i>Membership</i>		
CE-only memb.	2.53 (−0.09)	0.923 (−0.001)
dice-only memb.	2.66 (−0.22)	0.914 (−0.010)
<i>Training</i>		
no online target	12.22 (−9.78)	0.631 (−0.293)
two-stage training	2.55 (−0.11)	0.919 (−0.005)
UniCo (ours)	2.44	0.924

4.4. Ablations

We ablate core modules in heads, membership, and training, as summarized in Tab. 6, and train all variants for 200 epochs. Dropping the parameter head changes scores only slightly, but it remains necessary for assembly solvers that require explicit parameters (e.g., normals). Removing primitive-wise Chamfer slightly increases CD and lowers NC. For membership supervision, combining cross-entropy and Dice works best, while using only one increases CD and reduces

NC marginally. Training designs are most critical. Removing online target supervision is catastrophic, pushing CD to about five times that of the full model. Switching to a two-stage pipeline, where we first train the point pathway and then the primitive pathway, also increases CD and reduces NC.

5. Conclusion and Discussion

We rethought how primitives and points should interact for structured shape completion and introduced UniCo, a unified model that predicts assembly-ready primitives through primitive proxies. On mixed-type, plane-only, and real airborne LiDAR benchmarks, UniCo achieves state-of-the-art performance, establishing an effective recipe for structured 3D understanding from incomplete data.

Limitations. UniCo is tailored for shape completion aimed at primitive assembly and therefore prioritizes assembly-ready structure over pointwise fidelity. It is not intended for highly unstructured geometry where primitive abstraction provides limited benefit, and its final reconstruction quality depends on the downstream solver. Within this scope, however, UniCo reliably learns structures that assemble correctly.

Future work. Our method extends to richer primitive families. We observe that primitive proxies develop consistent proxy-level semantics, with specific proxies representing the same object parts even without explicit supervision. Future directions include exploiting these emergent correspondences for part-aware assembly and scaling UniCo to larger scenes.

Acknowledgments

This work was supported by TUM Georg Nemetschek Institute under the AI4TWINNING project. We thank Jing-En Jiang for support with PrimFit and Liangliang Nan for helpful discussions.

Appendix

In the appendix, we provide instructions for reproducing our results (Sec. A), detailed implementation settings (Sec. B), extended experimental analyses (Sec. C), and further details on the datasets (Sec. D) and metrics (Sec. E).

A. Reproducibility

The code repository and demo are publicly accessible via the project page¹. Detailed instructions for setup and running the code are described in the repository’s README.md file.

B. Implementation Details

The point pathway follows the AdaPoinTr backbone [70] with its default depth and hyperparameters. Input points are grouped into local neighborhoods, encoded with self-attention, and decoded from learned point queries. The decoder produces $U = 512$ shape features, which a lightweight reconstruction head expands into 8,192 completed points. As in AdaPoinTr, we use denoising queries during training for an auxiliary denoising loss and drop them at inference. The primitive pathway consumes the same U shape features. We use $K = 40$ learnable primitive queries, contextualized by a 4-layer Transformer decoder with 8 attention heads and a hidden size of 128. For each query, a prediction head outputs a primitive type, a soft mask over the 512 shape features, and 10 coefficients of a homogeneous quadric.

UniCo is implemented in PyTorch and optimized using the AdamW optimizer with an initial learning rate of 2×10^{-3} , a weight decay of 5×10^{-4} , and a learning rate decay of 0.9 every 20 epochs. During inference, primitives with confidence $s_k > 0.5$ are retained. For the loss terms in Eq. (12), we empirically set $\alpha_2 = 0.125$, $\alpha_3 = 1$ and $\lambda = 0.05$. To mitigate class imbalance, we set

$$\alpha_1 = \begin{cases} 0.05, & \text{if } c_g \neq \emptyset, \\ 0.01, & \text{otherwise.} \end{cases} \quad (\text{S1})$$

where c_g denotes the ground-truth primitive type. On *ABC-multi*, shapes contain on average about 8 primitives while we use $K = 40$ proxies, so the ratio for no-object vs. valid types roughly matches the expected proportion and keeps their aggregate loss contributions comparable. The impact of key hyperparameters is analyzed in Sec. C.

¹<https://unico-completion.github.io>

C. Additional Analyses

C.1. More Ablations

Number of primitive proxies. We vary the number of primitive proxies $K \in \{30, 40, 50\}$ and the no-object weight $\alpha_1(c_g = \emptyset)$ while keeping all other settings fixed. As reported in Tab. S1, $K = 40$ with a no-object weight of 0.01 achieves the best results.

Table S1. **Effect of proxy count and no-object weight.** Parameter counts (in millions) only include the primitive pathway $f_{\text{primitive}}$.

K	$\alpha_1(c_g = \emptyset)$	Params (M)	CD ↓	HD ↓	NC ↑	FR ↓
30	0.01	0.901	2.47	8.70	0.923	1.98
40	0.01	0.902	2.44	8.80	0.924	1.83
40	0.05	0.902	2.73	9.60	0.915	1.96
50	0.01	0.904	2.48	8.94	0.920	1.59

Confidence threshold. We assess the effect of the confidence threshold applied to the scores s_k in Eq. (14), varying the pruning value in $\{0.3, 0.5, 0.7\}$ at inference time. As summarized in Tab. S2, performance is fairly stable across thresholds, and $s_k > 0.5$ gives the best overall results.

Table S2. **Effect of confidence threshold.** Changing the pruning cutoff on s_k within a reasonable range has little effect on performance, while using $s_k > 0.5$ gives the best results.

$s_k >$	CD ↓	HD ↓	NC ↑	FR ↓
0.3	2.48	8.81	0.923	1.89
0.5	2.44	8.80	0.924	1.83
0.7	2.48	8.84	0.923	1.80

Analytic vs. fitted primitives. In Tab. S3, we compare primitives obtained directly from analytic quadric parameters with primitives obtained by fitting quadrics to the completed points. Since the assignments are identical, F1 and type accuracy remain unchanged. Analytic parameters achieve a lower axis error, whereas fitted primitives reduce the residual error and slightly improve coverage. For consistency with competing methods that rely on fitted primitives, the main paper reports the fitted variant.

Source	F1 ↑	Type ↑	Axis ↓	Res ↓	Cov ↑
Analytic	0.712	94.85	2.71	0.70	92.16
Fitted	0.712	94.85	3.29	0.55	92.41

Table S3. **Primitive quality for analytic vs. fitted sources.** Fitting quadrics to completed points improves residual error and coverage at a cost in axis error.

Projection. Tab. S4 compares UniCo with and without a projection-based post-processing step that projects completed

points onto their predicted primitives to enforce stricter planar geometry, with PaCo [10] as a reference. On both *ABC-plane* and *Building-PCC*, UniCo without projection already improves over PaCo, and projection brings only modest additional gains. For fairness, the main paper therefore reports UniCo without projection and treats the projected variant as an optional refinement for slightly sharper surfaces. Fig. S1 shows that PaCo tends to under-represent small primitives and fine details, whereas UniCo produces more uniform point distributions and cleaner, well-aligned primitive layouts across scales. Projection mainly sharpens surfaces and does not change this overall qualitative picture.

Table S4. **Effect of projection-based refinement.** UniCo already outperforms PaCo on *ABC-plane* and *Building-PCC*, and projection yields only marginal gains.

(a) <i>ABC-plane</i>				
Method	CD ↓	HD ↓	NC ↑	FR ↓
PaCo [10]	1.87	4.09	0.943	0.48
UniCo	1.69	4.28	0.953	0.69
UniCo (proj.)	1.67	4.29	0.955	0.55

(b) <i>Building-PCC</i>				
Method	CD ↓	HD ↓	NC ↑	FR ↓
PaCo [10]	4.89	10.74	0.932	0.54
UniCo	3.84	9.18	0.949	0.39
UniCo (proj.)	3.83	9.06	0.949	0.17

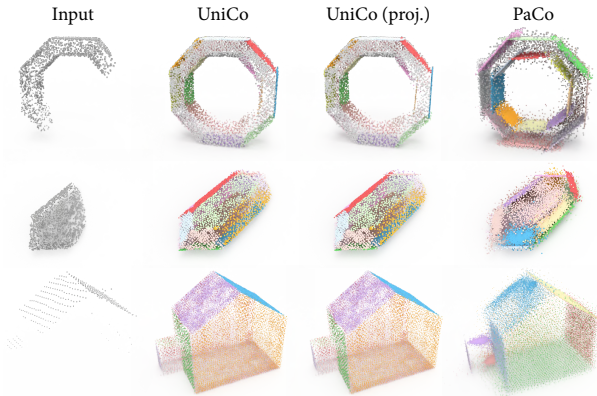


Figure S1. Qualitative primitive comparison on *ABC-plane* and *Building-PCC*. UniCo recovers more uniform point distributions and cleaner, well-aligned primitive structures.

Robustness across backbones. We additionally swap the point completion backbone f_{point} to PoinTr [69] or ODGNet [3]. UniCo retains *consistent* gains over the corresponding completion+extractor baselines. This shows that the improvements are driven by UniCo’s primitive pathway and persist across backbones.

Table S5. **Robustness across backbones.** UniCo retains consistent gains over the corresponding completion+extractor baselines.

Method	$f_{\text{point}} = \text{PoinTr [69]}$			$f_{\text{point}} = \text{ODGNet [3]}$		
	CD ↓	NC ↑	FR ↓	CD ↓	NC ↑	FR ↓
Compl.+Extr.	6.58	0.791	11.27	4.33	0.873	7.41
UniCo (ours)	2.64	0.915	2.49	2.47	0.922	0.31

C.2. Transferability

We train UniCo separately on the *ABC-multi* and *ABC-plane* and evaluate both on the plane-only split. To avoid data leakage, we exclude test shapes that also appear in the mixed-type training set. As shown in Tab. S6, the model trained on the mixed-type split exhibits only moderate degradation across all metrics and still achieves strong performance, indicating that UniCo transfers well from mixed-type to plane-only data.

Table S6. **Transferability.** UniCo trained on different datasets and evaluated on *ABC-plane*, excluding overlapping samples.

Training → Evaluation	CD ↓	HD ↓	NC ↑	FR ↓
ABC-plane → ABC-plane	1.70	4.35	0.953	1.16
ABC-multi → ABC-plane	2.06	5.36	0.942	2.13

Moreover, UniCo *generalizes* to unseen freeform geometries in *real* OmniObject3D scans [58] *without* training on them, by compactly approximating them with the available primitives, as shown in Fig. S2.

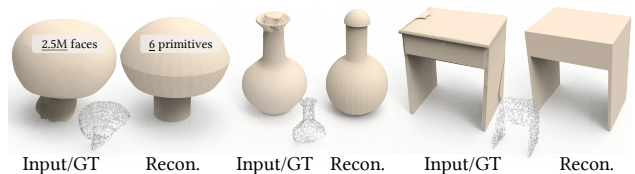


Figure S2. **OOD generalization via approximation.** UniCo trained on synthetic data with a fixed primitive set generalizes to real-world point clouds with unseen geometry by approximation.

C.3. Computational Efficiency

Tab. S7 reports per-scan runtimes on *ABC-plane*. UniCo processes each partial input in 27.6 ms end-to-end, roughly twice as fast as the strongest pointwise competitor, ODGNet [3], and faster than the structured competitor PaCo [10]. All other completion methods, except PaCo and UniCo, require an additional primitive extraction stage. To quantify this overhead, we evaluate RANSAC [42], HPNet [64], and PTv3 [59] on 100 randomly selected ABC-multi samples completed by ODGNet. UniCo is the fastest end-to-end pipeline.

Table S7. **Runtime and complexity.** All completion methods are measured on a single A40 GPU, excluding the first iteration to ensure steady-state measurements. For methods requiring primitive extraction, we additionally report RANSAC, HPNet, and PTv3 post-processing costs, evaluated on 100 random *ABC-multi* samples. “Total Params” and “Total Latency” refer to the parameter count and latency of the full pipeline. Params are reported in millions and all times are in milliseconds.

Method	Params	Latency	RANSAC [42]		HPNet [64]		PTv3 [59]	
			Total Params	Total Latency	Total Params	Total Latency	Total Params	Total Latency
AdaPoinTr [70]	32.5	23.9	32.5	124.9	33.8	1280.9	208.5	169.3
ODGNet [3]	11.5	53.6	11.5	154.6	12.8	1310.6	187.5	199.0
SymmComplete [63]	13.3	20.0	13.3	121.0	14.6	1277.0	189.4	165.4
PaCo [10]	41.4	29.8	41.4	29.8	41.4	29.8	41.4	29.8
UniCo (ours)	33.4	27.6	33.4	27.6	33.4	27.6	33.4	27.6

C.4. Failure cases

Typical failure modes involve missing small primitives and misclassified semantics, with examples shown in Fig. S3. These cases are overall rare and occur less often than in competing methods (see Tab. 3).

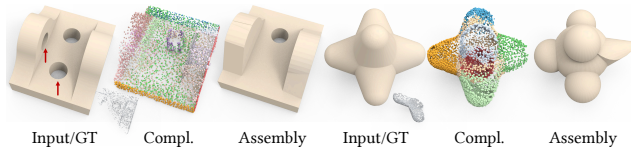


Figure S3. **Failure cases.** Typical failure cases involve missing small primitives and misclassified semantics.

D. Datasets

For *ABC-multi*, we randomly select 30,000 single-piece watertight CAD models from the ABC dataset [24], covering a broad spectrum of primitive configurations, from simple shapes with only a few primitives to complex assemblies with several tens of parts. Planes and cylinders dominate the primitive inventory, while cones and spheres provide additional geometric variety. This yields a diverse, structured benchmark for primitive-based completion. A quantitative summary is provided in Tab. S8.

In addition, we use *ABC-plane* [10], a plane-only subset of ABC, and *Building-PCC* [15], an airborne LiDAR dataset of roughly 50,000 urban buildings with noise and occlusions. These datasets complement *ABC-multi* by providing plane-only CAD assemblies and real-world scans for evaluation.

E. Metrics

For failed reconstructions, we follow the established protocol [10] and evaluate against the unit cube. Below we detail the additional primitive-level metrics used in Tab. 3, following established practice [16, 30, 36]. We denote a matched primitive pair by $(k^*, g^*) \in \mathcal{M}$:

Table S8. **Primitive statistics on *ABC-multi*.** Primitive counts, per-sample statistics, and type compositions for 30,000 CAD models.

Statistic	Value
Samples	30,000
Primitive instances	219,477
<i>Primitive instances by type</i>	
Plane	156,558 (71.3%)
Cylinder	55,349 (25.2%)
Cone	6,541 (3.0%)
Sphere	1,029 (0.5%)
<i>Primitives per sample</i>	
Min / median / max	2 / 7 / 38
25th / 75th percentile	4 / 10
Mean	7.32
<i>Type composition</i>	
Plane	5,800 (19.3%)
Cylinder	19 (0.1%)
Cone	87 (0.3%)
Sphere	15 (0.1%)
Plane+Cylinder	20,404 (68.0%)
Plane+Cone	448 (1.5%)
Plane+Sphere	139 (0.5%)
Cone+Cylinder	22 (0.1%)
Cylinder+Sphere	29 (0.1%)
Plane+Cone+Cylinder	2,538 (8.5%)
Plane+Cylinder+Sphere	339 (1.1%)
Plane+Cone+Cylinder+Sphere	121 (0.4%)
Other mixed combinations	39 (0.1%)

$$\begin{aligned}
 \mathbf{F1}: & \frac{1}{|\mathcal{M}|} \sum_{(k^*, g^*) \in \mathcal{M}} F_1(k^*, g^*), \\
 \mathbf{Type}: & \frac{1}{|\mathcal{M}|} \sum_{(k^*, g^*) \in \mathcal{M}} \mathbb{1}\{\hat{c}_{k^*} = c_{g^*}\}, \\
 \mathbf{Axis}: & \frac{\sum_{(k^*, g^*) \in \mathcal{M}} \mathbb{1}\{\hat{c}_{k^*} = c_{g^*}\} \arccos\langle n_{k^*}, n_{g^*} \rangle}{\sum_{(k^*, g^*) \in \mathcal{M}} \mathbb{1}\{\hat{c}_{k^*} = c_{g^*}\}}, \\
 \mathbf{Res}: & \frac{\sum_{(k^*, g^*) \in \mathcal{M}} \mathbb{1}\{\hat{c}_{k^*} \neq \emptyset\} \mathbb{E}_{\mathbf{x} \sim U(\theta_{g^*})} D(\mathbf{x}, \theta_{k^*})}{\sum_{(k^*, g^*) \in \mathcal{M}} \mathbb{1}\{\hat{c}_{k^*} \neq \emptyset\}}, \\
 \mathbf{Cov}: & \frac{\sum_{(k^*, g^*) \in \mathcal{M}} \mathbb{1}\{\hat{c}_{k^*} \neq \emptyset\} \mathbb{E}_{\mathbf{x} \sim U(\theta_{g^*})} \mathbb{1}\{D(\mathbf{x}, \theta_{k^*}) < \epsilon\}}{\sum_{(k^*, g^*) \in \mathcal{M}} \mathbb{1}\{\hat{c}_{k^*} \neq \emptyset\}},
 \end{aligned}$$

where $D(\mathbf{x}, \theta_{k^*})$ denotes the point-to-primitive distance, and $\mathbf{x} \sim U(\theta_{g^*})$ indicates uniform sampling over the bounded surface of the ground-truth primitive.

References

- [1] Jean-Philippe Bauchet and Florent Lafarge. Kinetic shape reconstruction. *ACM TOG*, 39(5):1–14, 2020. 1, 2, 5, 7, 8
- [2] Mario Botsch, Leif Kobbelt, Mark Pauly, Pierre Alliez, and Bruno Lévy. *Polygon mesh processing*. AK Peters/CRC Press, Natick, MA, USA, 2010. 1, 2
- [3] Pingping Cai, Deja Scott, Xiaoguang Li, and Song Wang. Orthogonal dictionary guided shape completion network for point cloud. In *AAAI*, pages 864–872, 2024. 2, 5, 6, 7, 8, 10, 11
- [4] Shaoyu Chen, Jiemin Fang, Qian Zhang, Wenyu Liu, and Xinggang Wang. Hierarchical aggregation for 3D instance segmentation. In *ICCV*, pages 15467–15476, 2021. 2
- [5] Zhaiyu Chen. abspy: A Python package for 3D adaptive binary space partitioning and modeling. *Journal of Open Source Software*, 2025. 2
- [6] Zhiqin Chen, Andrea Tagliasacchi, and Hao Zhang. BSP-Net: Generating compact meshes via binary space partitioning. In *CVPR*, pages 45–54, 2020. 2, 5, 6
- [7] Zhaiyu Chen, Hugo Ledoux, Seyran Khademi, and Liangliang Nan. Reconstructing compact building models from point clouds using deep implicit fields. *ISPRS Journal of Photogrammetry and Remote Sensing*, 194:58–73, 2022. 2
- [8] Zhikai Chen, Fuchen Long, Zhaofan Qiu, Ting Yao, Wengang Zhou, Jiebo Luo, and Tao Mei. AnchorFormer: Point cloud completion from discriminative nodes. In *CVPR*, pages 13581–13590, 2023. 2
- [9] Zhaiyu Chen, Yilei Shi, Liangliang Nan, Zhitong Xiong, and Xiao Xiang Zhu. PolyGNN: Polyhedron-based graph neural network for 3D building reconstruction from point clouds. *ISPRS Journal of Photogrammetry and Remote Sensing*, 218: 693–706, 2024. 2
- [10] Zhaiyu Chen, Yuqing Wang, Liangliang Nan, and Xiao Xiang Zhu. Parametric point cloud completion for polygonal surface reconstruction. In *CVPR*, pages 11749–11758, 2025. 2, 5, 7, 8, 10, 11
- [11] Bowen Cheng, Alex Schwing, and Alexander Kirillov. Per-pixel classification is not all you need for semantic segmentation. In *NeurIPS*, pages 17864–17875, 2021. 4
- [12] Angela Dai, Charles R. Qi, and Matthias Nießner. Shape completion using 3D encoder-predictor CNNs and shape synthesis. In *CVPR*, pages 5868–5877, 2017. 2
- [13] Ruoxi Deng, Chunhua Shen, Shengjun Liu, Huibing Wang, and Xinru Liu. Learning to predict crisp boundaries. In *ECCV*, pages 562–578, 2018. 4
- [14] Philipp Erler, Paul Guerrero, Stefan Ohrhallinger, Niloy J Mitra, and Michael Wimmer. Points2Surf: Learning implicit surfaces from point clouds. In *ECCV*, pages 108–124, 2020. 2
- [15] Weixiao Gao, Ravi Peters, and Jantien Stoter. Building-PCC: Building point cloud completion benchmarks. *ISPRS Annals of the Photogrammetry, Remote Sensing and Spatial Information Sciences*, pages 179–186, 2024. 5, 11
- [16] Haoxiang Guo, Shilin Liu, Hao Pan, Yang Liu, Xin Tong, and Baining Guo. ComplexGen: CAD reconstruction by B-Rep chain complex generation. *ACM TOG*, 2022. 6, 11
- [17] Xiaoguang Han, Zhen Li, Haibin Huang, Evangelos Kalogerakis, and Yizhou Yu. High-resolution shape completion using deep neural networks for global structure and local geometry inference. In *ICCV*, pages 85–93, 2017. 2
- [18] Jiahui Huang, Hao-Xiang Chen, and Shi-Min Hu. A neural Galerkin solver for accurate surface reconstruction. *ACM TOG*, 41(6):1–16, 2022. 2
- [19] Zhangjin Huang, Yuxin Wen, Zihao Wang, Jinjuan Ren, and Kui Jia. Surface reconstruction from point clouds: A survey and a benchmark. *IEEE TPAMI*, 2024. 2
- [20] Jingen Jiang, Mingyang Zhao, Shiqing Xin, Yanchao Yang, Hanxiao Wang, Xiaohong Jia, and Dong-Ming Yan. Structure-aware surface reconstruction via primitive assembly. In *ICCV*, 2023. 1, 2, 5, 6
- [21] Li Jiang, Hengshuang Zhao, Shaoshuai Shi, Shu Liu, Chi-Wing Fu, and Jiaya Jia. Pointgroup: Dual-set point grouping for 3D instance segmentation. In *CVPR*, pages 4867–4876, 2020. 2
- [22] Adrien Kaiser, Jose Alonso Ybanez Zepeda, and Tamy Boubekeur. A survey of simple geometric primitives detection methods for captured 3D data. In *Computer Graphics Forum*, pages 167–196. Wiley Online Library, 2019. 2
- [23] Michael Kazhdan and Hugues Hoppe. Screened Poisson surface reconstruction. *ACM TOG*, 32(3):1–13, 2013. 2
- [24] Sebastian Koch, Albert Matveev, Zhongshi Jiang, Francis Williams, Alexey Artemov, Evgeny Burnaev, Marc Alexa, Denis Zorin, and Daniele Panozzo. ABC: A big CAD model dataset for geometric deep learning. In *CVPR*, pages 9601–9611, 2019. 1, 5, 11
- [25] Harold W Kuhn. The Hungarian method for the assignment problem. *Naval research logistics quarterly*, 2(1-2):83–97, 1955. 4
- [26] Jean Lahoud, Bernard Ghanem, Marc Pollefeys, and Martin R Oswald. 3D instance segmentation via multi-task metric learning. In *ICCV*, pages 9256–9266, 2019. 2
- [27] Xin Lai, Yuhui Yuan, Ruihang Chu, Yukang Chen, Han Hu, and Jiaya Jia. Mask-attention-free yufomer for 3D instance segmentation. In *ICCV*, pages 3693–3703, 2023. 2
- [28] Eric-Tuan Lê, Minhyuk Sung, Duygu Ceylan, Radomir Mech, Tamy Boubekeur, and Niloy J Mitra. CPFN: Cascaded primitive fitting networks for high-resolution point clouds. In *ECCV*, pages 7457–7466, 2021. 2
- [29] Sangho Lee, Hayun Lee, and Dongkun Shin. ProxyFormer: Nyström-based linear transformer with trainable proxy tokens. In *AAAI*, pages 13418–13426, 2024. 2
- [30] Lingxiao Li, Minhyuk Sung, Anastasia Dubrovina, Li Yi, and Leonidas J Guibas. Supervised fitting of geometric primitives to 3D point clouds. In *CVPR*, pages 2652–2660, 2019. 2, 6, 11
- [31] Pu Li, Jianwei Guo, Xiaopeng Zhang, and Dong-Ming Yan. SECAD-Net: Self-supervised CAD reconstruction by learning sketch-extrude operations. In *CVPR*, pages 16816–16826, 2023. 2
- [32] Yangyan Li, Oliver van Kaick, Hao Zhang, Ariel Shamir, Daniel Cohen-Or, and Baoquan Chen. GlobFit: Consistently fitting primitives by discovering global relations. *ACM TOG*, 30(4):52:1–52:12, 2011. 2
- [33] Zihao Liang, Zihao Li, Songcen Xu, Mingkui Tan, and Kui Jia. Instance segmentation in 3D scenes using semantic superpoint tree networks. In *ICCV*, pages 2783–2792, 2021. 2

- [34] Fangzhou Lin, Yun Yue, Songlin Hou, Xuechu Yu, Yajun Xu, Kazunori D Yamada, and Ziming Zhang. Hyperbolic chamfer distance for point cloud completion. In *ICCV*, pages 14595–14606, 2023. 1, 2
- [35] Fangzhou Lin, Yun Yue, Ziming Zhang, Songlin Hou, Kazunori Yamada, Vijaya Kolachalama, and Venkatesh Saligrama. InfoCD: A contrastive chamfer distance loss for point cloud completion. *NeurIPS*, 36:76960–76973, 2023. 1, 2
- [36] Yujia Liu, Anton Obukhov, Jan Dirk Wegner, and Konrad Schindler. Point2CAD: Reverse engineering CAD models from 3D point clouds. In *CVPR*, pages 3763–3772, 2024. 2, 5, 6, 11
- [37] Jiahao Lu, Jiacheng Deng, Chuxin Wang, Jianfeng He, and Tianzhu Zhang. Query refinement transformer for 3D instance segmentation. In *CVPR*, 2023. 2
- [38] Liangliang Nan and Peter Wonka. PolyFit: Polygonal surface reconstruction from point clouds. In *ICCV*, pages 2353–2361, 2017. 1, 2, 5, 7, 8
- [39] Charles R. Qi, Hao Su, Kaichun Mo, and Leonidas J. Guibas. PointNet: Deep learning on point sets for 3D classification and segmentation. In *CVPR*, pages 652–660, 2017. 2
- [40] Charles R. Qi, Li Yi, Hao Su, and Leonidas J. Guibas. PointNet++: Deep hierarchical feature learning on point sets in a metric space. In *NeurIPS*, 2017. 2
- [41] Daxuan Ren, Jianmin Zheng, Jianfei Cai, Jiatong Li, Haiyong Jiang, Zhongang Cai, Junzhe Zhang, Liang Pan, Mingyuan Zhang, Haiyu Zhao, et al. CSG-Stump: A learning friendly CSG-like representation for interpretable shape parsing. In *ICCV*, pages 12478–12487, 2021. 2
- [42] Ruwen Schnabel, Roland Wahl, and Reinhard Klein. Efficient RANSAC for point-cloud shape detection. *Comput. Graph. Forum*, 26(2):214–226, 2007. 2, 5, 6, 10, 11
- [43] Jonas Schult, Francis Engelmann, Alexander Hermans, Or Litany, Siyu Tang, and Bastian Leibe. Mask3D: Mask transformer for 3D semantic instance segmentation. In *Proceedings of the IEEE International Conference on Robotics and Automation*, 2023. 2, 4
- [44] Gopal Sharma, Difan Liu, Subhransu Maji, Evangelos Kalogerakis, Siddhartha Chaudhuri, and Radomír Měch. ParSeNet: A parametric surface fitting network for 3D point clouds. In *ECCV*, pages 261–276, 2020. 2
- [45] Raphael Sulzer and Florent Lafarge. Concise plane arrangements for low-poly surface and volume modelling. *ECCV*, 2024. 1, 2, 5, 7, 8
- [46] Jiahao Sun, Chunmei Qing, Junpeng Tan, and Xiangmin Xu. Superpoint transformer for 3D scene instance segmentation. In *AAAI*, pages 2393–2401, 2023. 2
- [47] Ramesh Ashok Tabib, Dikshit Hegde, Tejas Anvekar, and Uma Mudenagudi. DeFi: detection and filling of holes in point clouds towards restoration of digitized cultural heritage models. In *ICCVW*, pages 1603–1612, 2023. 1
- [48] Junshu Tang, Zhijun Gong, Ran Yi, Yuan Xie, and Lizhuang Ma. LAKe-Net: Topology-aware point cloud completion by localizing aligned keypoints. In *CVPR*, pages 1726–1735, 2022. 2
- [49] Keneni W Tesema, Lyndon Hill, Mark W Jones, Muneeb I Ahmad, and Gary KL Tam. Point cloud completion: A survey. *IEEE TVCG*, 2023. 2
- [50] Hugues Thomas, Charles R. Qi, Jean-Emmanuel Deschaud, Beatriz Marcotequi, François Goulette, and Leonidas J. Guibas. KPConv: Flexible and deformable convolution for point clouds. In *ICCV*, pages 6411–6420, 2019. 2
- [51] Theodore Tsesmelis, Luca Palmieri, Marina Khoroshiltseva, Adeela Islam, Gur Elkin, Ofir I Shahar, Gianluca Scarpellini, Stefano Fiorini, Yaniv Ohayon, Nadav Alali, et al. Re-assembling the past: The RePAIR dataset and benchmark for real world 2D and 3D puzzle solving. *NeurIPS*, 37:30076–30105, 2024. 1
- [52] Shubham Tulsiani, Hao Su, Leonidas J Guibas, Alexei A Efros, and Jitendra Malik. Learning shape abstractions by assembling volumetric primitives. In *CVPR*, pages 2635–2643, 2017. 2
- [53] Jacob Varley, Chad DeChant, Adam Richardson, Joaquín Ruales, and Peter Allen. Shape completion enabled robotic grasping. In *IEEE/RSJ international conference on intelligent robots and systems*, pages 2442–2447. IEEE, 2017. 1
- [54] Thang Vu, Kookhoi Kim, Tung M Luu, Thanh Nguyen, and Chang D Yoo. Softgroup for 3D instance segmentation on point clouds. In *CVPR*, pages 2708–2717, 2022. 2
- [55] Yue Wang, Yongbin Sun, Ziwei Liu, Sanjay E. Sarma, Michael M. Bronstein, and Justin M. Solomon. Dynamic graph CNN for learning on point clouds. *ACM TOG*, 38(5):146:1–146:12, 2019. 2
- [56] Yuqing Wang, Zhaiyu Chen, and Xiao Xiang Zhu. Learning generalizable shape completion with SIM(3) equivariance. *NeurIPS*, 2025. 6, 7
- [57] Tong Wu, Liang Pan, Junzhe Zhang, Tai Wang, Ziwei Liu, and Dahua Lin. Density-aware chamfer distance as a comprehensive metric for point cloud completion. *arXiv preprint arXiv:2111.12702*, 2021. 1, 2
- [58] Tong Wu, Jiarui Zhang, Xiao Fu, Yuxin Wang, Jiawei Ren, Liang Pan, Wayne Wu, Lei Yang, Jiaqi Wang, Chen Qian, et al. Omniobject3D: Large-vocabulary 3D object dataset for realistic perception, reconstruction and generation. In *CVPR*, pages 803–814, 2023. 10
- [59] Xiaoyang Wu, Li Jiang, Peng-Shuai Wang, Zhijian Liu, Xihui Liu, Yu Qiao, Wanli Ouyang, Tong He, and Hengshuang Zhao. Point Transformer V3: Simpler, faster, stronger. In *CVPR*, 2024. 5, 6, 10, 11
- [60] Zhirong Wu, Shuran Song, Aditya Khosla, Fisher Yu, Linguang Zhang, Xiaoou Tang, and Jianxiong Xiao. 3D ShapeNets: A deep representation for volumetric shapes. In *CVPR*, pages 1912–1920, 2015. 2
- [61] Xuhao Xiang, Chaoping Zhang, Zizhuang Wei, and Shenghua Gao. SnowflakeNet: Point cloud completion by snowflake point deconvolution with skip-transformer. In *ICCV*, pages 5499–5509, 2021. 2
- [62] Haozhe Xie, Hongxun Yao, Shangchen Zhou, Jiageng Mao, Shengping Zhang, and Wenxiu Sun. GRNet: Gridding residual network for dense point cloud completion. In *ECCV*, pages 365–381, 2020. 2, 5, 6, 7
- [63] Hongyu Yan, Zijun Li, Kunming Luo, Li Lu, and Ping Tan. SymmCompletion: High-fidelity and high-consistency point

- cloud completion with symmetry guidance. In *AAAI*, pages 9094–9102, 2025. [2](#), [5](#), [6](#), [7](#), [8](#), [11](#)
- [64] Siming Yan, Zhenpei Yang, Chongyang Ma, Haibin Huang, Etienne Vouga, and Qixing Huang. HPNet: Deep primitive segmentation using hybrid representations. In *ICCV*, pages 2753–2762, 2021. [2](#), [5](#), [6](#), [10](#), [11](#)
- [65] Xuejun Yan, Hongyu Yan, Jingjing Wang, Hang Du, Zhihong Wu, Di Xie, Shiliang Pu, and Li Lu. FBNet: Feedback network for point cloud completion. In *ECCV*, pages 676–693, 2022. [2](#)
- [66] Yaoqing Yang, Chen Feng, Yiru Shen, and Dong Tian. FoldingNet: Point cloud auto-encoder via deep grid deformation. In *CVPR*, pages 206–215, 2018. [2](#)
- [67] Fenggen Yu, Zhiqin Chen, Manyi Li, Aditya Sanghi, Hooman Shayani, Ali Mahdavi-Amiri, and Hao Zhang. CAPRI-Net: Learning compact CAD shapes with adaptive primitive assembly. In *CVPR*, pages 11768–11778, 2022. [2](#), [6](#)
- [68] Mulin Yu and Florent Lafarge. Finding good configurations of planar primitives in unorganized point clouds. In *CVPR*, pages 6367–6376, 2022. [2](#), [5](#)
- [69] Xumin Yu, Yongming Rao, Ziyi Wang, Zuyan Liu, Jiwen Lu, and Jie Zhou. PoinTr: Diverse point cloud completion with geometry-aware transformers. In *ICCV*, pages 12498–12507, 2021. [1](#), [2](#), [5](#), [6](#), [7](#), [10](#)
- [70] Xumin Yu, Yongming Rao, Ziyi Wang, Jiwen Lu, and Jie Zhou. AdaPoinTr: Diverse point cloud completion with adaptive geometry-aware transformers. In *IEEE TPAMI*, pages 14114–14130, 2023. [2](#), [3](#), [5](#), [6](#), [7](#), [8](#), [9](#), [11](#)
- [71] Wentao Yuan, Tejas Khot, David Held, Christoph Mertz, and Martial Hebert. PCN: Point completion network. In *2018 international conference on 3D vision (3DV)*, pages 728–737, 2018. [1](#), [2](#)
- [72] Ruibin Zhao, Xinhai Liu, Jiancheng Li, and Hongbo Fu. SeedFormer: Patch seeds based point cloud completion with up-sample transformer. In *CVPR*, pages 11967–11976, 2022. [2](#)
- [73] Chaoda Zheng, Feng Wang, Naiyan Wang, Shuguang Cui, and Zhen Li. Towards flexible 3D perception: Object-centric occupancy completion augments 3D object detection. In *NeurIPS*, 2024. [1](#)
- [74] Zhe Zhu, Liangliang Nan, Haoran Xie, Honghua Chen, Jun Wang, Mingqiang Wei, and Jing Qin. CSDN: Cross-modal shape-transfer dual-refinement network for point cloud completion. *IEEE TVCG*, 2023. [2](#)